JBC RESEARCH ARTICLE

Distinct roles of the major binding residues in the cation-binding pocket of the melibiose transporter MelB

Received for publication, March 9, 2024, and in revised form, May 11, 2024 Published, Papers in Press, May 31, 2024,
https://doi.org/10.1016/j.jbc.2024.107427

Parameswaran Hariharan[1,‡], **Amirhossein Bakhtiiari**[2,‡], **Ruibin Liang**[2,*], **and Lan Guan**[1,*]

From the [1]*Department of Cell Physiology and Molecular Biophysics, Center for Membrane Protein Research, School of Medicine, Texas Tech University Health Sciences Center, Lubbock, Texas, USA;* [2]*Department of Chemistry and Biochemistry, Texas Tech University, Lubbock, Texas, USA*

Reviewed by members of the JBC Editorial Board. Edited by Karen Fleming

Salmonella enterica **serovar Typhimurium melibiose permease ($MelB_{St}$) is a prototype of the major facilitator superfamily (MFS) transporters, which play important roles in human health and diseases. $MelB_{St}$ catalyzed the symport of galactosides with Na^+, Li^+, or H^+ but prefers the coupling with Na^+. Previously, we determined the structures of the inward- and outward-facing conformation of $MelB_{St}$ and the molecular recognition for galactoside and Na^+. However, the molecular mechanisms for H^+- and Na^+-coupled symport remain poorly understood. In this study, we solved two x-ray crystal structures of $MelB_{St}$, the cation-binding site mutants D59C at an unliganded apo-state and D55C at a ligand-bound state, and both structures display the outward-facing conformations virtually identical as published. We determined the energetic contributions of three major Na^+-binding residues for the selection of Na^+ and H^+ by free energy simulations. Transport assays showed that the D55C mutant converted $MelB_{St}$ to a solely H^+-coupled symporter, and together with the free-energy perturbation calculation, Asp59 is affirmed to be the sole protonation site of $MelB_{St}$. Unexpectedly, the H^+-coupled melibiose transport exhibited poor activities at greater bulky ΔpH and better activities at reversal ΔpH, supporting the novel theory of transmembrane-electrostatically localized protons and the associated membrane potential as the primary driving force for the H^+-coupled symport mediated by $MelB_{St}$. This integrated study of crystal structure, bioenergetics, and free energy simulations, demonstrated the distinct roles of the major binding residues in the cation-binding pocket of $MelB_{St}$.**

The secondary active transporters, including symporters or antiporters, play important roles in physiology and pathology. The major facilitator superfamily (MFS) transporters contain many cation-coupled symporters, most of which couple to either H^+ or Na^+ electrochemical gradient. The melibiose permease of *Salmonella* enterica serovar Typhimurium ($MelB_{St}$), a member of MFS transporters, catalyzes the symport of a galactopyranoside with either of H^+, Li^+, or Na^+, which makes MelB as a unique system for studying cation-coupled transport mechanisms (1–12). In humans, the Na^+-coupled lipids transporter (MFSD2A) expressed in the major barriers, such as the blood-brain barrier or blood-retina barrier, plays a critical role in the uptake of essential lipids into these neural tissues (9, 10, 13). These transporters shared the same cation-binding site as the bacterial MelB (9–11, 13, 14), but the molecular mechanisms were much less characterized. MelB, as the best-studied system for this group of transporters, is useful for expanding our knowledge base of cation-coupled transport mechanisms.

Two crystal structures with a bound sugar analog have been reported for a cation-binding site mutant D59C $MelB_{St}$ in its outward-facing conformation, which provided essential information on the determinants for the sugar substrate specificity (8) (Fig. 1*A*). Recently, a Na^+-bound inward-facing conformation of the WT $MelB_{St}$ has been determined by cryoEM single-particle analysis, which reveals the Na^+ specificity determinants (11) (Fig. 1*B*). Binding affinity measurements of melibiose and Na^+ or Li^+ to $MelB_{St}$ in the absence or presence of the other have been extensively carried out *via* isothermal titration calorimetry (ITC), which revealed positive cooperativity between the sugar and coupling cation with $MelB_{St}$ (15). The cooperativity number, defined as the ratio in the K_d values of melibiose and cation in the absence or presence of the other, reflects the coupling efficiency for transporting melibiose with a coupling action. For Na^+ or Li^+, the cooperativity number is approximately 8 (15) and 5 (6), respectively, which are significantly greater than that between melibiose and H^+, with a number of less than 2 based on the effect of sugar on the H^+ affinity (15). The structures with bound sugar or Na^+ reveal that the two binding pockets are in close proximity with no direct overlap (6, 11), but the molecular basis for the coupling between the sugar and cation is still elusive.

It is noteworthy that the sugar-binding affinity, in addition to being sensitive to the binding of the coupling cation and its identity, is conformation-dependent (11). It is usually quite technically challenging to determine the substate-binding affinity for a specific conformation of a transporter because of the conformational variability. The conformation dependency of the sugar-binding affinity of $MelB_{St}$ was obtained by using an inward-facing conformation-specific nanobody Nb725 (11). By isolating the inward-facing state, both the experimental

‡ Co-first author.
* For correspondence: Lan Guan, Lan.Guan@ttuhsc.edu; Ruibin Liang, rliang@ttu.edu.

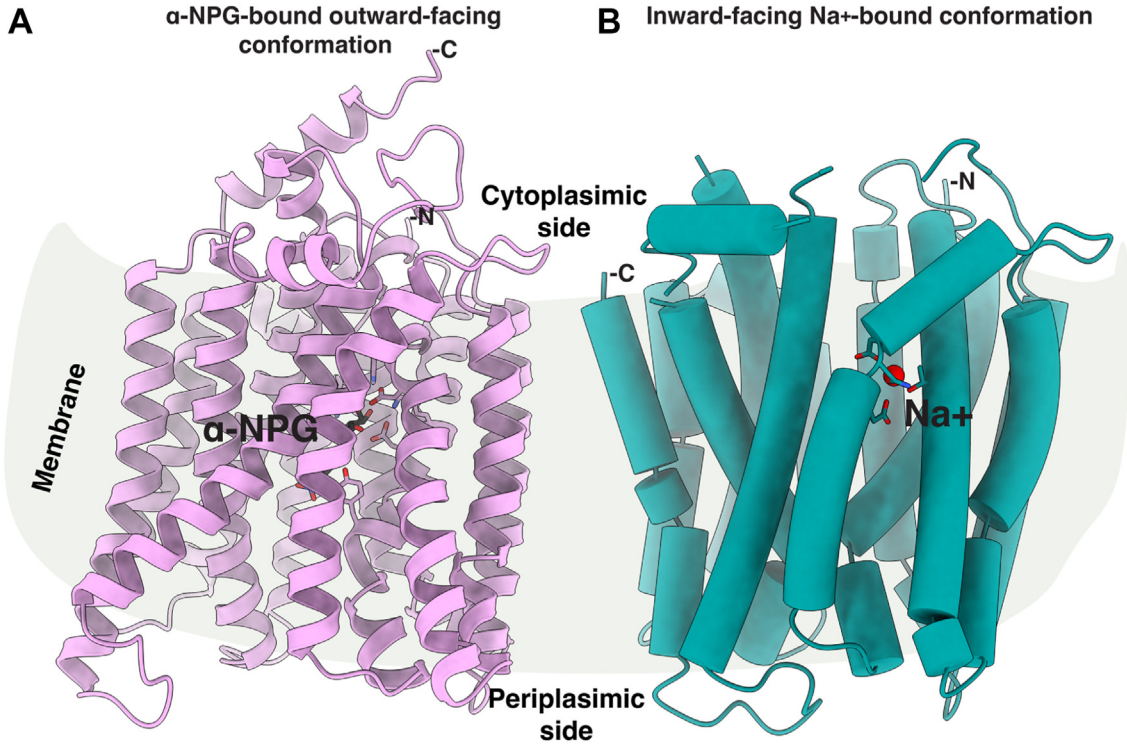

Figure 1. Structures of MelB$_{St}$. *A*, the ligand-bound outward-facing conformation [PDB ID 7L17]. The cartoon helical representation of the x-ray crystal structure of D59C MelB$_{St}$ mutant with bound α-NPG (8). The sugar-binding sidechains are highlighted in the *sticks* and an α-NPG molecule is colored in *black*. *B*, the inward-facing structure of MelB$_{St}$ [PDB ID 8T60] (16). Cylindrical helices representation of the cryoEM structure of the WT MelB$_{St}$ bound with Na$^+$. The Na$^+$-binding sidechains are highlighted in the *sticks* and Na$^+$ is colored *red*. The middle loop and the C-terminal tail are disordered. The sidedness of the membrane is indicated. For both structures, the helices II and XI were placed at the front, and the N-terminus was placed at the right side.

sugar-binding assay and cryoEM structure support a low-affinity state of the sugar-binding pocket at the intracellular sugar-releasing state (11, 14). This observation allows for assigning the measured sugar binding affinity as the outward-facing or occluded states.

Remarkably, the Na$^+$ binding to the inward-facing conformation remains unchanged (11, 14). All-atom molecular dynamics simulations revealed the virtually identical configurations of this cation-binding pocket at either inward- or outward-facing conformation (16). These results support the stepped binding kinetic model for melibiose/Na$^+$ symport at a sequential order of Na$^+$ binding first and its release following the sugar release at the other surface, which was constructed based on transport assays, such as efflux and exchange, in a combination of mutants and sugar-binding assay in both MelB of *Escherichia coli* and MelB$_{St}$ (4, 7, 17–20).

Both structural and functional studies support that the stoichiometry of the substrate, cation, and transporter is unity. This single cation site for Na$^+$ also accommodates H$^+$ or Li$^+$ and the Na$^+$ binding to MelB$_{St}$ is competitively inhibited by Li$^+$ (4) or H$^+$ (15). The stoichiometry number of the coupling H$^+$ was verified by measuring the buffer protonation upon the binding of Na$^+$ in a set of buffer systems at varying pH values. Structurally, the cation-binding site is formed by two helices within only the N-terminal 6-helix bundle or N-lobe, which might be the structural basis for the unchanged affinity between the outward- and inward-facing states. The Na$^+$ binding involves two negatively charged residues, Asp55 and Asp59 (helix II), and two polar residues, Asn58 (helix II) and Thr121 (helix IV). In this shared cation-binding pocket, only Asp55 or Asp59 could serve as a protonation site. The absolute dissociation constant for H$^+$, *i.e.*, the p*K*a value, has been experimentally determined to be in a slightly acidic range of 6.25 and 6.5 in the absence or presence of melibiose (15).

Asp59 has been suggested to be the protonation site in MelB$_{St}$ for the H$^+$-coupled transport (7, 8) and MelB$_{Ec}$ (21, 22). The extensive functional analysis and structural studies show that the D59C mutant loses the active transport of melibiose coupled to the translocation of either Na$^+$, Li$^+$, or H$^+$, but retains the capability of melibiose transport driven by the melibiose concentration gradient (7, 8, 23). D59C mutant loses the binding to Na$^+$ or Li$^+$ (15), and it is a uniporter mutant of MelB$_{St}$.

D55C MelB$_{St}$ also loses the binding affinity with Na$^+$ or Li$^+$ and is unable to mediate Na$^+$- or Li$^+$-coupled melibiose active transport. Different from the D59C mutant, the D55C mutant retains the H$^+$-coupled melibiose active transport activity (7), which excludes the role of Asp55 in the H$^+$ binding. The single-site mutagenesis at the Thr121 showed that Ala or Pro replacement only selectively eliminates the Na$^+$ binding and Na$^+$-coupled melibiose transport but retains the full transport activity coupled to Li$^+$ or H$^+$ (14).

All obtained data suggested the Asp59 as the sole protonation site; however, the molecular basis for the H$^+$-coupled transport is unclear. The D55C mutation is an excellent tool for isolating the H$^+$-coupling transport mode to gain insights into the H$^+$-coupled transport mediated by a Na$^+$-coupled transporter

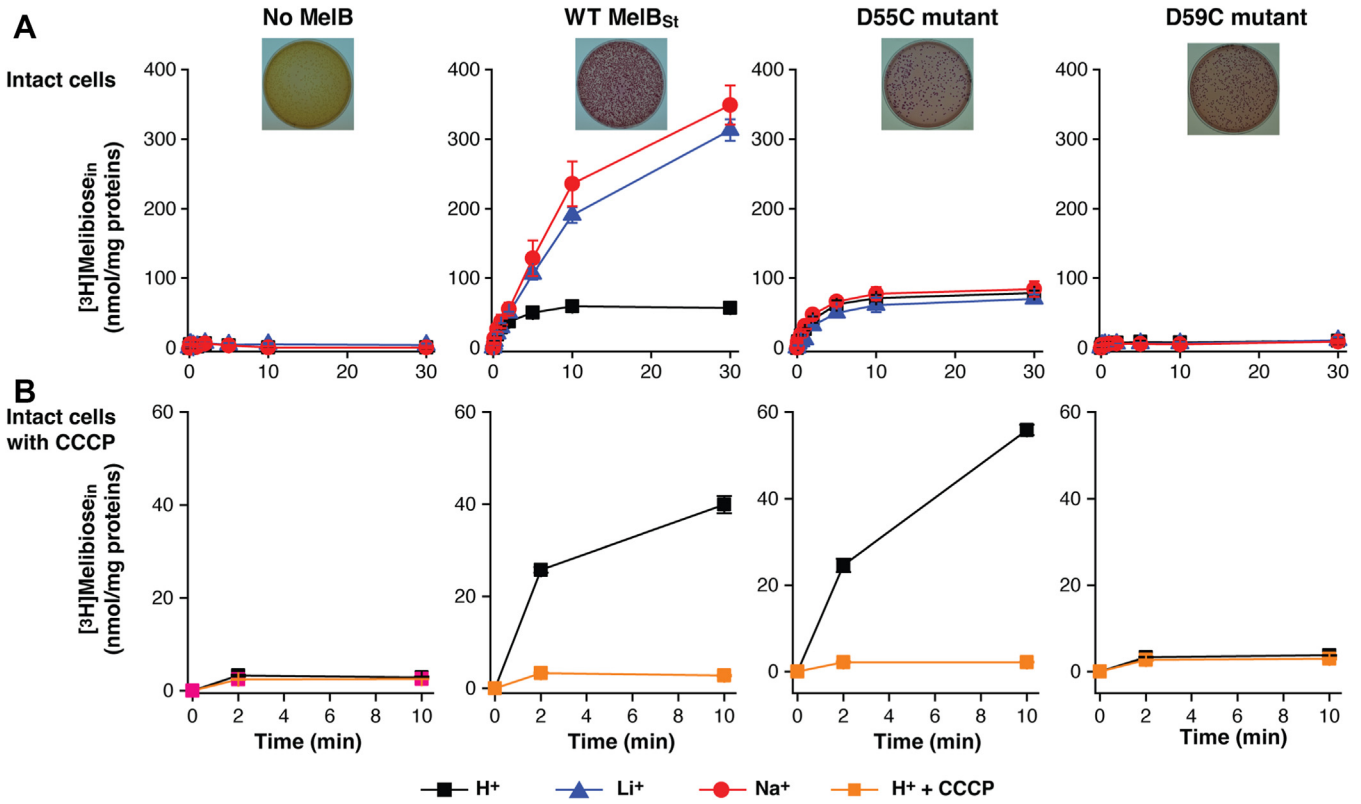

Figure 2. Intact cell transport assay. *E. coli* DW2 cells (*melA*$^+$*B*$^-$, *lacZ*$^-$*Y*$^-$) expressing the plasmid-encoding WT MelB$_{St}$ mutants D55C or D59C were prepared for [^{3}H]melibiose transport assay. *A*, melibiose transport coupled to H$^+$, Na$^+$, or Li$^+$. Melibiose transport was conducted at 0.4 mM (specific activity of 10 mCi/mmol) in the presence of 20 mM Na$^+$ or Li$^+$ or the absence of Na$^+$ and Li$^+$ as described in Methods. The results were plotted as mean ± SE, test number = 2 to 4. The cells without MelB were the negative control. *Inset*, melibiose fermentation assay. The cells were also plated onto the MacConkey agar plate containing 30 mM melibiose as the sole carbohydrate source and neutral red dye as the pH indicator. The plates were photographed after 16 to 18 h incubation at 37 °C. *Yellow colonies*, no melibiose fermentation; magenta colonies, good melibiose fermentation. *B*, CCCP effect. The cells were pre-incubated with 10 μM CCCP, and the H$^+$-coupled melibiose uptake was measured at zero, 2 m, or 10 m. The results were plotted as mean ± SE, test number = 3.

without potentially contaminating Na$^+$ interference. Here, we report two crystal structures that include the Apo D59C and the ligand-bound D55C mutants and analyze their structures in detail. Furthermore, we performed free energy calculations using molecular dynamics (MD) to quantify the energetic contributions of each of the three side chains (Asp55, Asp59, and Thr121) to the binding of Na$^+$ or H$^+$, respectively. All data further support the conclusion that Asp59 is the protonation site of MelB$_{St}$ and Asp55 and Asp59 are the major contributors to the Na$^+$-binding affinity. Unexpectedly, the external pH effects on the sugar transport with MelB$_{St}$ showed poor activities at greater bulky ΔpH and better activities at reversal ΔpH. The high activity at alkaline pH can not be interpreted using Peter Mitchell's canonical chemiosmosis theory but can be explained using the revised chemiosmosis theory, which added a third term naming transmembrane-electrostatically localized protons (TELP) (24–26). Our data support that the membrane potential is the primary driving force for the H$^+$-coupled uptake.

Results

Melibiose transport activity

The results of melibiose active transport mediated by the WT MelB$_{St}$ and the mutants D55C and D59C with intact cells have been published previously (7, 8, 23). The data are reproducible and re-plotted for comparison with the melibiose fermentation data. At a melibiose concentration of 0.4 mM, the WT MelB$_{St}$ expressed in *E. coli* DW2 cells (*mel*A$^+$*B*$^-$, *lacZ*$^-$*Y*$^-$) accumulated melibiose in the presence of Na$^+$ or Li$^+$ at least 6-fold higher than that in the absence of Na$^+$ or Li$^+$ (Fig. 2*A*, red or blue, respectively). The melibiose transport in the absence of Na$^+$ and Li$^+$ has been annotated as H$^+$-coupled transport (Fig. 2*A*, black). On the MacConkey agar plate containing melibiose as the sole carbohydrate source and neutral red dye as pH indicator for the acidification yielded by melibiose fermentation, the *E. coli* DW2 cells with no MelB grew yellow colonies indicating no melibiose fermentation (Fig. 2*A*, inset) and the presence of WT MelB$_{St}$ changed the color of colonies and agar to magenta indicating good melibiose-downhill transport and fermentation (Fig. 2*A*, inset). The D55C mutant selectively lost the symport activities with Na$^+$ or Li$^+$, but fully retained the H$^+$-coupled melibiose symport activity (Fig. 2*A*). The initial rates of transport and the steady-state accumulation between the WT and the D55C mutant are indistinguishable. The D55C MelB$_{St}$ mutant also reproducibly fermented the melibiose as the WT did (Fig. 2*A*, inset). The uniporter D59C mutant lost all symport activity but retained the melibiose fermentation as published previously (Fig. 2*A*) (8).

To further test the melibiose uptake coupled to the electrochemical H$^+$ gradient, the melibiose transport assay was conducted with the cells pre-incubated with the proton

ionophore, the uncoupler carbonyl cyanide m-chlorophenylhydrazone (CCCP) at 10 μM (Fig. 2*B*). Clearly, CCCP completely inhibited the H^+-coupled transport activity in both of WT and the D55C mutant, confirming the H^+-coupled melibiose transport mediated by the D55C $MelB_{St}$ and the WT.

Binding affinity determination by the isothermal titration calorimetry

The D55C mutant has been shown to lose the Na^+ binding (7, 15). With isothermal titration calorimetry (ITC), titration of Na^+ or Li^+ at even higher concentrations in the absence or presence of a saturating concentration of melibiose further confirmed that the D55C mutation eliminated the binding of Na^+ and Li^+ (Fig. 3, *A* and *B*).

A qualitative Trp to dansyl-galactoside (D^2G) FRET assay has suggested that the D55C mutation binds melibiose and D^2G (7). The quantitative ITC measurements showed that melibiose binding to D55C mutant in the absence of Na^+ or Li^+ exhibits a K_d value of 5.82 ± 0.46 mM (Table 1; Fig. 3*C*), which is significantly lower than the published value of 9.28 ± 0.23 mM for the WT (8) under the same condition ($p < 0.01$). In the presence of Na^+, the WT exhibited an 8.51-fold decrease in the K_d value for melibiose, but no change was observed with the D55C mutant, which is consistent with no binding of Na^+ or Li^+ (7).

The ITC measurement was also used to measure the binding of the hydrophobic ligand α-NPG to the D55C mutant and the estimated K_d value is 15.06 ± 1.86 μM with no Na^+ effect, which is lower than that of WT (Table 1; Fig. 3*D*). Consistent with the melibiose binding, the α-NPG affinity for the D55C mutant did not increase in the presence of Na^+.

pH effects on the H^+-coupled melibiose transport and binding

To understand how external pH affected the H^+-coupled symport activity, melibiose transport was carried out in 8 extracellular bulky pH values at an interval of 0.5 units (5.5, 6.0, 6.5, 7.0, 7.5, 8.0, 8.5, or 9.0) (Fig. 4*A*). With the WT, at the acidic pH of 5.5, the cells accumulated melibiose poorly, but the uptake gradually increased along with an increase in external pH values. The transport activity became undistinguishable between external pH 7.5 to 9.0. With the D55C mutant, the external pH effect on the transport activity exhibited a pattern similar to the WT, *i.e.*, weaker activity at the acidic pH range and greater at the alkaline pH range, and the steady-state accumulation levels are slightly higher than that in the WT. The CCCP effect at varied external pH was conducted at zero, 2 m, and 10 m time points, and the transport activities were completely abolished at all tested pH

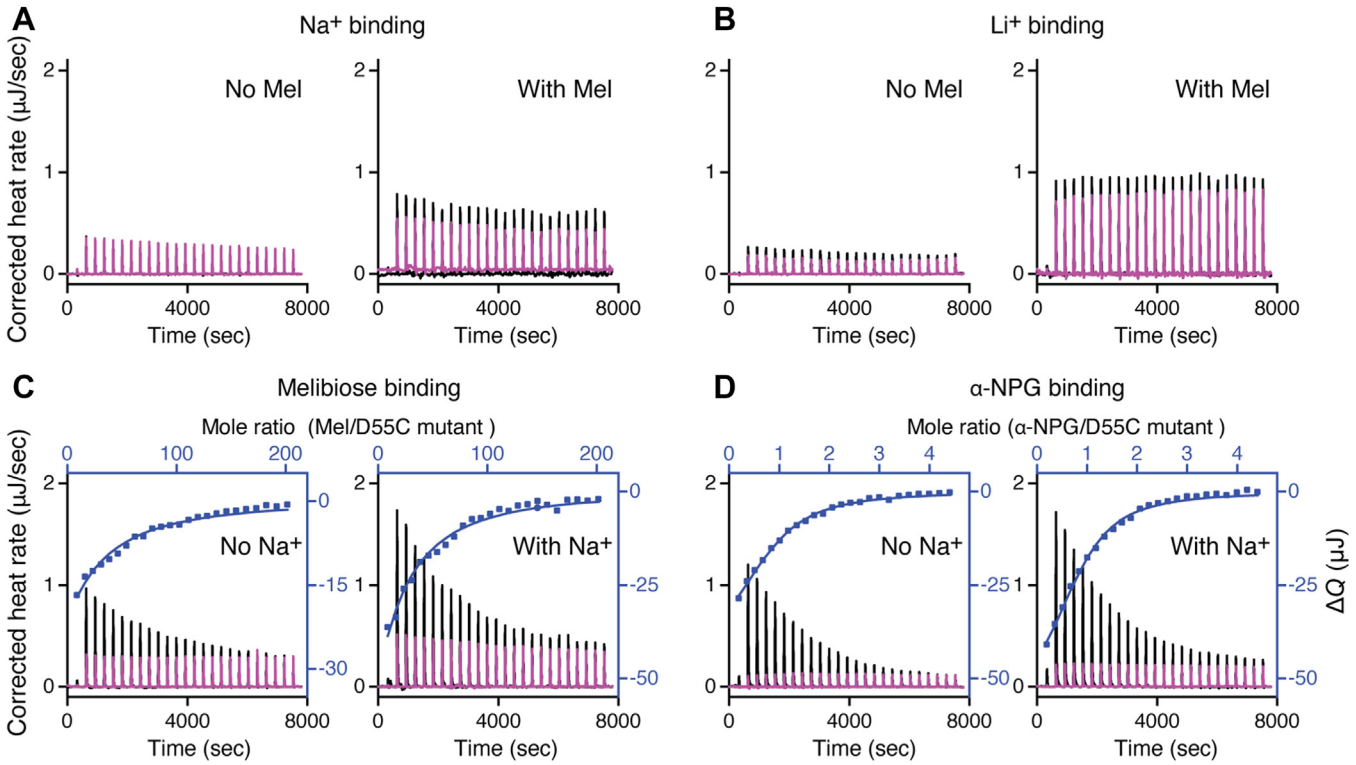

Figure 3. Binding assay *via* ITC. All ITC binding assays to D55C $MelB_{St}$ mutant were conducted with ITC calorimeters (TA Instruments) at 25 °C. *A*, Na^+ binding in the absence or presence of melibiose. The 40 mM NaCl concentration was used for titration, which is 8-fold greater or 20-fold greater than that used for the WT in the absence or presence of the melibiose, respectively. *B*, Li^+ binding in the absence or presence of melibiose. The 40 mM LiCl concentration was used for titration, which is 8-fold greater or 20-fold greater than that used for the WT in the absence or presence of the melibiose, respectively. *C*, melibiose binding in the absence or presence of Na^+. *D*, α-NPG binding in the absence or presence of Na^+. The thermogram was plotted as the baseline-corrected heat rate (μJ/s; left axis) *versus* time (*bottom axis*) for the titrant to $MelB_{St}$ (*black*) or to buffer (*red*) under an identical scale. The heat change ΔQ (μJ; filled blue symbol) was plotted against the ligand/D55C mutant $MelB_{St}$ molar ratio (*top/right axes*). The figures only showed the representative data; the results are presented in Table 1.

Table 1
K_d of sugar binding to $MelB_{St}$

$MelB_{St}$	pH	Na^+ (mM)	Melibiose (mM)	Affinity change	α-NPG (μM)	Affinity change
WT[a]	7.5	/	9.28 ± 0.23[bc] (n = 3)	+8.51-fold	43.20 ± 0.62 (n = 2)	+ 1.68-fold
	7.5	100	1.09 ± 0.06 (n = 4)		25.69 ± 4.42 (n = 2)	
D55C	7.5	/	5.82 ± 0.46[c] (n = 2)	+1.14-fold	15.06 ± 1.86[c] (n = 2)	+1.11
	7.5	100	5.09 ± 0.15 (n = 2)		13.54 ± 1.38 (n = 2)	
WT	6.25	/	6.19 ± 0.59[d] (n = 2)	+1.37-fold		
WT	8.5	/	8.50 ± 0.21[d] (n = 3)			

[a] data published in reference of (8).
[b] sem, standard error; n, the number of tests.
[c] unpaired t test, $p < 0.01$.
[d] unpaired t test, $p < 0.05$.

conditions (Fig. 4*A*, orange curves). The D59C mutant showed no active transportive activity at all the testing pH values, indistinguishable from the control cells with no MelB.

Since the transport activity was affected by the external pH value, the pH effect on sugar-binding was conducted at an acidic and an alkaline pH with two different methods. The ITC measurements were used to determine the melibiose-binding affinity with purified WT $MelB_{St}$ in a Na^+-free buffer at pH 6.25 and 8.5 as described in the method (Fig. 4*B*). The obtained K_d values at pH 6.25 and 8.5 are 6.19 ± 0.59 and 8.50 ± 0.21 mM, respectively (Table 1). The K_d value at acidic pH was even less than 2-fold lower than that in pH 8, indicating that the sugar binding at acidic conditions is not the main reason for the poor transport.

This result also provided the missing data for constructing the thermodynamic cycle between the binding of sugar and H^+, as we constructed for melibiose with other coupling cations Na^+ or Li^+ (8, 15). The pH effect on melibiose affinity is similar to the sugar effect on the protonation of $MelB_{St}$, where the absolute $K_{D(H+)}$ value was from 0.56 μM to 0.26 μM in the presence of melibiose (15). All support the positive cooperativity between the co-transported solutes.

The well-established Trp to dansyl galactoside FRET assay (2, 4) was used to detect the dansyl-galactoside binding with right-side-out (RSO) membrane vesicles expressed the WT and D55C mutants prepared in 100 mM KPi buffer adjusted to pH 6.0 or 8.0, respectively (Fig. 4*C*). The intensity changes of the WT or D55C mutant in either pH were similar, supporting the conclusion from the ITC measurements that the melibiose-binding affinity is less affected by the pH change, which is largely different from the effects induced by Na^+ or Li^+ (6, 15). Thus, it was reinforced that the reduced transport activities observed in both WT and the D55C mutants do not stem from decreased sugar binding affinity.

Crystal structure determination

As reported, the purified D55C and D59C $MelB_{St}$ in detergent undecyl-β-D-maltopyranoside (UDM) solution exhibited improved thermostabilities (15). The crystal structures of D59C mutant bound with α-NPG and DDMB have been published (8). Here we report the structures of apo D59C and DDMB-bound D55C $MelB_{St}$ mutants, which were determined by molecular replacement (Table 2), modeled from positions 2 to 454 or 2 to 256 without a gap (Fig. 5, *A* and *B*), refined to a resolution of 3.0 Å and 3.18 Å, respectively. The two structures exhibit an RMSD value of 0.263 Å and are virtually identical to the published DDMB-bound [PDB ID 7L16] or α-NPG-bound D59C (PDB ID 7L17) structures at RMSD values of less than 0.4 Å. In both structures, a PEG molecule was modeled between the helices IX and XII at the cytoplasmic side, which could imply a potential lipid-binding site.

The Apo D59C and D55C structures showed virtually identical galactoside-binding pockets (Fig. 5*C*). In the D55C structure, the galactosyl moiety of bound DDMB exhibits a similar pose to that in the D59C bound with either DDMB or α-NPG. The densities of the 11-carbon tail were disordered and only 2 carbons were modeled. The glucosyl moiety pose is different from that in the D59C structure. The Na^+-binding pocket in both crystal structures is nearly identical to the previously published D59C structures, with a Cys present at positions of either Asp55 or Asp59, respectively (Fig. 5, *C* and *D*). In comparison with the Na^+-bound WT $MelB_{St}$ cryoEM structure (Fig. 6), both the DDMB-bound D55C and apo D59C $MelB_{St}$ mutants exhibited loosely packed side chains in this cation-binding pocket due to the absence of Na^+ (the D55C structure was removed for clarity).

Effect of single-site mutations on Na^+-binding affinity

The three well-characterized single-site mutants D55C, D59C, or T121A were subjected to free energy calculations to quantitatively analyze the effects of the mutation on the Na^+ binding affinity. The change in the Na^+-binding affinity upon mutation was evaluated by the free-energy perturbation (FEP) simulations (Fig. 7*A*; Table 3; Table S1) and the construction of the thermodynamics cycle. The $\Delta G_{Na+\text{-unbound}}$ or $\Delta G_{Na+\text{-bound}}$ reflect the free energy change upon mutating the WT to a given mutant in the Na^+-unbound or Na^+-bound states of $MelB_{St}$, respectively. Based on the thermodynamic cycle (Fig. 7*A*), the difference between these two free energy changes ($\Delta\Delta G_{Na+\text{-binding}} = \Delta G_{\text{mutation, Na+-bound state}} - \Delta G_{\text{mutation, Na+-unbound state}}$) equals the change in the Na^+-binding free energy induced by the mutation. In other words, $\Delta\Delta G_{Na+\text{-binding}}$ reflects how much the mutation perturbs the binding affinity of Na^+. More positive $\Delta\Delta G$ values indicate greater reductions in the cation-binding affinity due to the mutation. The D59C mutation yielded the greatest destabilization in Na^+ binding with a $\Delta\Delta G$ value of 10.5 ± 0.3 kcal/mol, followed by the D55C

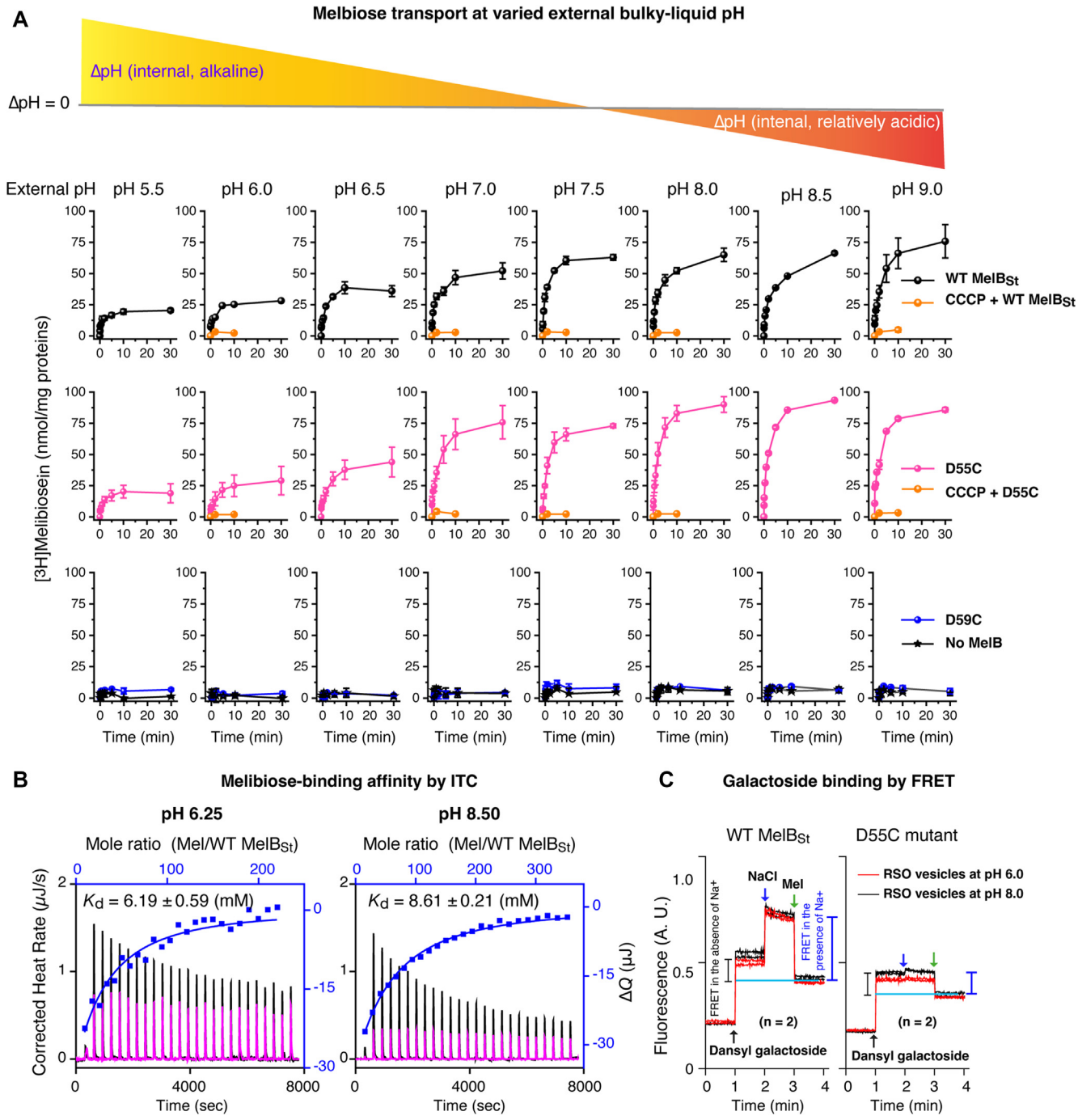

Figure 4. pH effects on melibiose transport and binding. *A*, external pH effect on melibiose transport. Protein expression of the WT $MelB_{St}$, D55C, and D59C mutants is described in Figure 2. After the third washing with 50-mL buffer of 100 mM KP_i, pH 7.5, the cells were aliquoted into eight groups and further washed with 50-mL KP_i buffer at pH value adjusted from 5.5 to 9.0 at an interval of 0.5 value and 10 mM $MgSO_4$. The cell pellets collected from centrifugation were resuspended in the same buffer at a given pH value. The transport assay was conducted at 0.4 mM melibiose (specific activity, 10 mCi/mmol) in the absence of Na^+ and Li^+. The bar on the top reflects the relative pH gradients between external and internal bulky pH. The CCCP effect at 5 different pH conditions was conducted for a shorter time course (zero, 2 m, and 10 m) and plotted within the corresponding panels colored in orange as labeled. All data were presented in mean values with SE, and the testing number was 2 to 4 times. *B*, melibiose binding by ITC at pH 6.25 or 8.5. The WT $MelB_{St}$ (80 μM) in 20 mM Tris-HCl, 100 mM choline chloride, 10% glycerol, and 0.035% UDM at pH either 6.25 or 8.5 were titrated with the buffer-matched melibiose solutions at 50 mM or 80 mM, respectively. The control experiments were conducted with the same buffer solutions devoid of $MelB_{St}$ protein. The figures only showed the representative data and the results were presented in Table 1. *C*, galactoside binding with RSO membrane vesicles. The WT or D55C $MelB_{St}$ RSO vesicles were pre-equilibrated in 100 mM KPi buffer at pH 6.0 or 8.0 and used to measure the Trp→D^2G FRET by sequentially adding 10 μM D^2G, 50 mM NaCl, and >120 mM melibiose, as indicated by the *arrows*. The duplicated tests for each condition were plotted in the figure. The changes indicated by the *gray* or *blue bar* showed the FRET intensity from bound D^2G in the absence or presence of Na^+ as labeled.

Table 2
Crystallographic Data collection and refinement statistics

	D55C $MelB_{St}$ with DDMB	Apo D59C $MelB_{St}$
Data collection PDB ID	8FQ9	8FRH
Space group	P 31 2 1	P 31 2 1
Cell dimensions		
a, *b*, *c* (Å)	127.225,127.225,104.042	127.93 127.93 104.52
α, β, γ (°)	90 90,120	90 90,120
Resolution (Å)	24.56–3.00	34.82–3.15
R_{sym} or R_{merge}	0.119 (3.463)	0.149 (3.088)
$I/\sigma I$	16.8 (0.8)	21.2 (1.3)
Completeness (%)	99.8 (100)	99.50 (100.00)
Redundancy	13.3 (13.0)	21.8 (22.3)
Refinement		
Resolution (Å)	20–3.00 (3.07–3.00)	20–3.18 (3.27–3.18)
No. reflections	19,788 (1944)	16,869 (1659)
R_{work}/R_{free}	0.263/0.283	0.260/0.286
No. of non-hydrogen atoms	3616	3577
Protein	3575	3561
Ligand (1PE)	16	16
Ligand (DDMB)	25	/
Water	0	0
Average B-factor	114.73	115.05
Protein	114.32	115.02
Ligand/ion	118.32	122.17
R.m.s. deviations		
Bond lengths (Å)	0.002	0.003
Bond angles (°)	0.557	0.511

Each data was collected from a single crystal. Values in parentheses are for the highest-resolution shell.

mutation with a $\Delta\Delta G$ value of 8.6 ± 0.3 kcal/mol, and the T121A mutation with a least $\Delta\Delta G$ value of 6.7 ± 0.1 kcal/mol. The data are consistent with the notion that all side chains are important but the two carboxyl groups on Asp55 and Asp59 play major roles in the Na^+ binding in $MelB_{St}$.

The effect of mutations on the protonation of Asp55 or Asp59

Among the two titratable residues, a largely elevated p*K*a value of 8.75 for Asp59 was estimated by PROPKA (14). The pKa estimation of Asp55 obtained from a consistent simulation protocol using PROPKA reveals a value of 4.0, in the expected range for an Asp side chain in bulk solution, which further confirms that Asp59 is the sole protonation site in $MelB_{St}$. To determine how the Cys mutation at Asp55 affects the protonation of Asp59 and *vice versa*, free-energy perturbation simulations were applied to calculate the $\Delta\Delta G_{\text{proton binding at Asp59}}$ (Table 3). Based on the thermodynamic cycle, this $\Delta\Delta G$ value equals the difference between the mutation-introduced free energy change in the H^+-unbound and H^+-bound states of $MelB_{St}$, with the proton-binding site being either Asp59 or Asp55 (Fig. 7*B*). Thus, this $\Delta\Delta G$ value reflects the change of the proton-binding affinity of either residue due to the mutation of the other. More positive values indicate weaker proton-binding affinities or larger inhibition of the proton binding introduced by a mutation. The FEP simulation results showed that the H^+-binding affinity of Asp59 in the D55C mutant is only 2.0 ± 0.2 kcal/mol lower than the WT, *i.e.*, the p*K*a value is estimated to decrease by 1.5 units. Compared to the effect on the Na^+ binding, the effect of the D55C mutation on the proton-binding affinity of Asp59 is much smaller (Table 3); therefore, the Asp59 can still serve as a protonation site in this mutant. In contrast, the D59C mutation leads to a decrease of the H^+-binding affinity of Asp55 by 5.1 ± 0.4 kcal/mol, about a 3.7-unit decrease in the p*K*a value. The data support that the D55C mutant retains the H^+-coupled symport activity mediated by the protonation and deprotonation of the Asp59 residue (Fig. 6). In contrast, the D59C mutation eliminates this activity due to the removal of the sole proton-binding site (Asp59), and the remaining Asp55 is incapable of serving as a protonation site because its original low proton-binding affinity in the WT is further decreased by 5.1 ± 0.4 kcal/mol due to the Cys mutation at Asp59.

Discussion

There are two well-conserved acidic residues in the cation-binding pocket of MelB, and those two positions have also been well-studied in the past by several laboratories using varied methods (5, 7, 8, 21, 23, 27). Cys or Ala mutants on the strictly conserved Asp59 lose the binding of Na^+ and Li^+, as well as the melibiose active transport coupled to the Na^+, Li^+, or H^+. However, these mutants still mediate melibiose translocation driven by melibiose concentration gradient (Fig. 2*A*, inset), converting the WT $MelB_{St}$ symporter to a uniporter (8).

The D55C mutant also loses the Na^+ and Li^+ binding and the melibiose active transport coupled to the Na^+ or Li^+ but maintained the melibiose concentration gradient-drive melibiose transport as shown by the melibiose fermentation assay (Fig. 2*A* inset), similar to the D59C mutant. Interestingly, the single-Cys D55C mutant at a Cys-less background with endogenous 8 Cys residues replaced with Ala, showed poor melibiose fermentation activity (23). The protein stability of the Cys-less $MelB_{St}$ is not as good as the WT, which might result in poor melibiose transport and fermentation. Intriguingly, the D55C $MelB_{St}$ retains the H^+-coupled symport activity and the uncoupler CCCP abolished the activities of both WT and the D55C mutant (Fig. 2*B*). The crystal structures of both D55C and D59C mutants in the absence or presence of a ligand reveal a virtually identical cation-binding pocket except for the mutations and sidechain poses of major Na^+-binding players (Figs. 5 and 6).

To further characterize the individual role of the three well-studied side chains (Asp 55, Asp59, and Thr121) in this shared cation-binding pocket, the FEP simulations in combination with the construction of thermodynamic cycles were utilized to estimate the mutational effects of these residues on the affinities for Na^+ or H^+ in $MelB_{St}$. The results showed that all three side chains are important for the Na^+ binding. The single-site mutations at the two negatively charged Asp59 and Asp55 residues make greater destabilization for the Na^+ binding, which supports the experimentally established conclusion that the Na^+ binding is primarily stabilized by the carboxyl groups in the side chains of Asp55 and Asp59, especially Asp59 (7, 11, 15).

PROPKA calculations suggest that the estimated p*K*a values of Asp59 and Asp55 are 8.7 (14) and 4.0, respectively. The

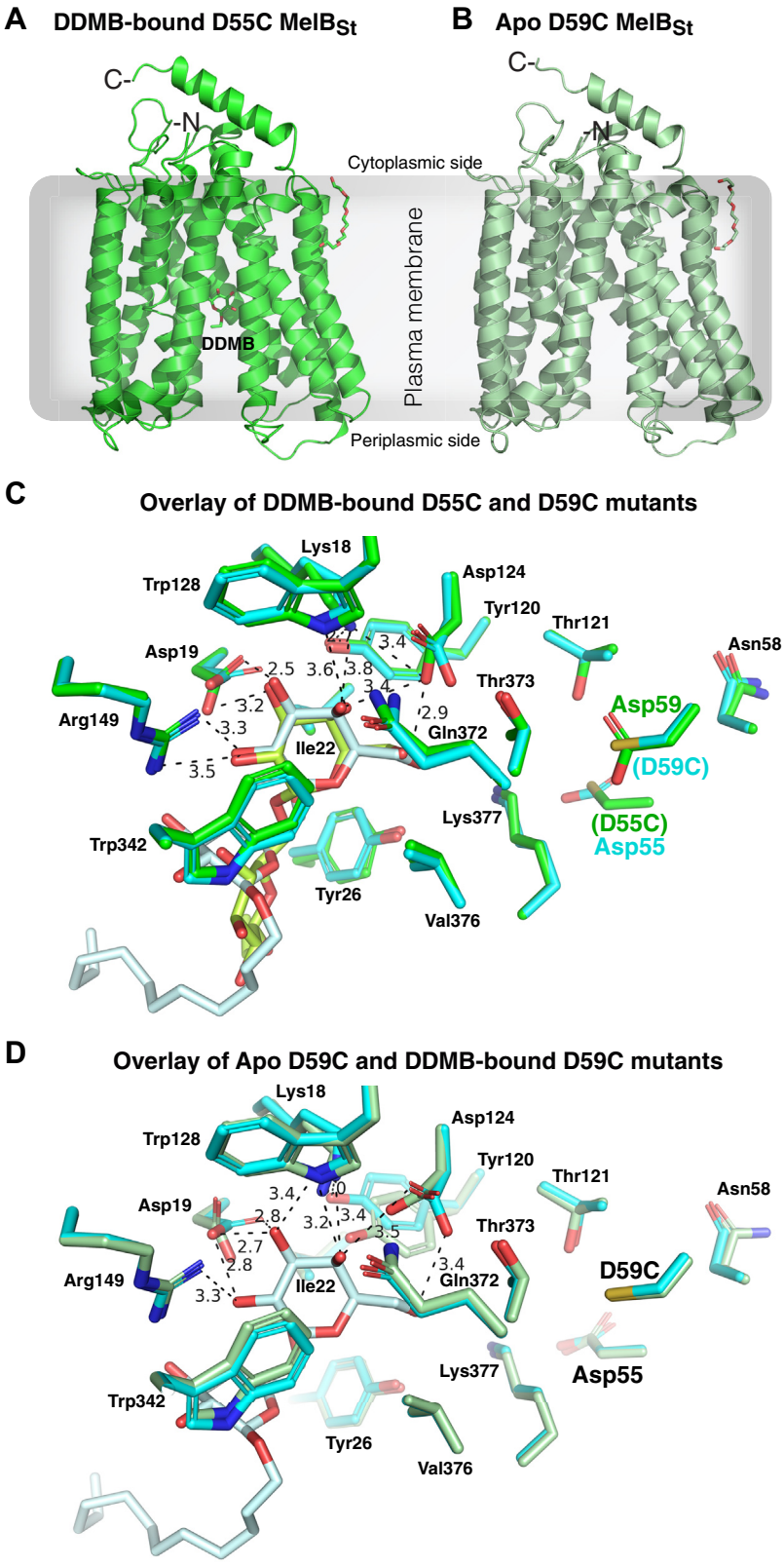

Figure 5. Crystal structures of the D55C and D59C MelB$_{St}$ mutants. *A*, D55C mutant bound with DDMB refined to a resolution of 3.0 Å. The structure was shown in cartoon representation in *green* and DDMB with 2-carbon tail is shown in the stick and labeled. *B*, D59C mutant at apo state refined to a resolution of 3.18 Å. The structure was shown in cartoon representation in *light green*. The helices V and VIII were placed at the middle and N-terminus on the *left side* for both structures. One PEG molecule interacted with the cytoplasmic side of helix IX in both structures. The sidedness of the membrane is indicated. *C*, the specificity determinant pockets for the sugar substrates and the coupling cations. The DDMB-bound D55C mutant was overlaid on the DDMB-bound D59C mutant [PDB 7L16]. The DDMB-binding residues are shown in the sticks, and the DDMB molecules were *colored green* (D55C mutant) and pale cyan (D59C mutant), respectively. The cation-binding residues (positions 55, 58, 59, and 121) were shown in the stick. *D*, overlay of the apo D59C and DDMB-bound D59C mutants. The DDMB-binding residues are shown in the sticks, and the DDMB molecules were colored *green* (D55C mutant) and pale *cyan* (D59C mutant), respectively. The cation-binding residues (Asp55, Ans58, D59C, and Thr121) were shown in the *stick*.

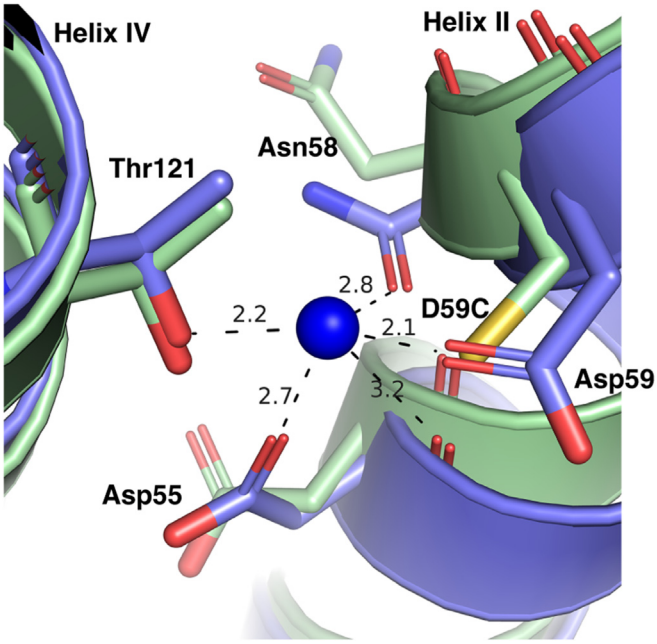

Figure 6. Superimposed Na^+-binding pocket of the WT and mutants. The N-terminal helices of the Na^+-bound inward-facing cryoEM structure of the WT $MelB_{St}$ [PDB ID 8T60] were aligned on the Apo D59C mutant. The Na^+-binding residues were shown in the stick, and the distance of Na^+ coordinates was indicated with *dashed lines* (Å). Helices II and IV were labeled.

highly elevated p*K*a value of Asp59 is consistent with its major role as the proton-binding site (8), and p*K*a value of Asp55 at the normal range also supported that Asp55 is not involved in the protonation of the WT $MelB_{St}$. When Thr121 is mutated to Ala, proton-binding affinity at Asp59 is unchanged (14). The free energy calculation (Table 3; Fig. 7*B*) showed that the proton-binding affinity of Asp59 is only slightly reduced by 2.0 ± 0.2 kcal/mol by D55C mutation, largely retaining the capability of Asp59 for binding proton. In contrast, the proton-binding affinity of Asp55 is reduced by 5.1 ± 0.4 kcal/mol by D59C mutation, leaving no proton-binding site in the D59C mutant. This computational result is consistent with the experimental observation that the D59C mutation effectively eliminates the proton-coupled transport activity, in addition to the Na^+-and Li^+-coupled modes. The D55C mutation selectively eliminates the Na^+ and Li^+ binding and converts $MelB_{St}$ to a solely H^+-coupled symporter.

We have reported that the sugar-binding affinity is conformation-dependent, but both the inward- and outward-facing conformations of $MelB_{St}$ exhibited similar cation-binding pockets (8, 11, 14). This has raised an important question about the cation-releasing mechanisms during sugar/cation symport cycling. Interestingly, Na^+ binding in $MelB_{St}$ can be selectively eliminated readily by a single-site mutation on either Asp55 or Thr121 position without significant effect on H^+, or even no effect on Li^+ in the case of Thr121 mutations, as well as the corresponding coupled transport (8, 14). The Na^+ coordinates likely required stringent positioning of each side-chain. We are attempting to explain that the Asp55 side chain rotamer movement after releasing the sugar could release the Na^+ to the cavity. Further, the Na^+-binding affinity is greater than the intracellular Na^+ concentrations, implying that the membrane potential (inside negative) is needed for promoting the Na^+ departure from the internal cavity to the cytoplasmic solution. This is consistent with the previous study showing that is required for Na^+-coupled melibiose uptake (4).

The D55C $MelB_{St}$ mutant with only the H^+-coupling mode is a useful tool to study the H^+-coupled transport without interference from potentially contaminated Na^+. When conducting the H^+-coupled transport at external acidic pH values (pH < 7.0), it is surprising that both WT and the D55C mutant $MelB_{St}$ exhibited largely reduced transport activities (Fig. 4). The melibiose binding assays using two methods with purified proteins or RSO membrane vesicles showed that the sugar-binding affinity at both acidic and alkaline pH is reasonably well-preserved, which excluded the possibility of poor sugar binding at acidic pH values. Normally, *E. coli* cells maintain a relatively constant intracellular pH value of 7.6 (28–30). Even at the extracellular pH of 5.5 and 9.0, the intracellular pH was determined as 7.4 and 7.8, respectively (28). Thus, the decrease in the external pH should increase the pH gradient across the cell membrane (ΔpH, inside alkaline). If the transport rate were coupled to the bulk-liquid ΔpH (inside alkaline), greater transport activities should have been expected at lower external pH values. In contrast, the data revealed that the greater the ΔpH value (such as external liquid pH 5.5), the poorer the transport activity, which does not support the bulk-liquid ΔpH as a major driving force for the H^+-coupled melibiose uptake mediated by $MelB_{St}$. On the other hand, greater transport activities were observed at reversal ΔpH conditions (external liquid pH ≥ 8.0). All the data support that the H^+/melibiose symport is mainly coupled to $\Delta\Psi$.

It is well known that an H^+-coupled secondary active transport is coupled to the total free energy as a form of the electrochemical H^+ gradient ($\Delta\tilde{\mu}_{H+}$), also named proton motive force (31, 32). The $\Delta\tilde{\mu}_{H+}$ at least consists of two compensating terms: $\Delta\Psi$ and ΔpH. It is also known that the increase in ΔpH decreases the $\Delta\Psi$ value, and *vice versa* (33). The poor transport activities obtained at external acidic pH values or greater ΔpH (internal alkaline) could stem from the reduced $\Delta\Psi$ and deprotonation.

Another unexpected result is the strong and CCCP-sensitive transport activity in the alkaline pH range (pH > 8.0) with both WT and the D55C mutant. The experimentally determined p*K*a value of the cation pocket, *i.e.*, the Asp59, is approximately 6.5 with purified $MelB_{St}$ (15). The previous buffer protonation study by measuring enthalpic change at different buffer systems reveals that at pH 8.2, nearly all $MelB_{St}$ is deprotonated (15). The possibility that this phenomenon arises from Na^+ contaminations can be undoubtedly excluded since this D55C mutant does not bind Na^+. Thus, the observed H^+-coupled active melibiose transport at low external H^+ concentration or revered pH gradients (inside, relatively acidic) indicated that the WT and D55C mutant $MelB_{St}$ carried by the live-intact cells can be protonated even at an external pH 9.0 value. The data support a recent novel theory over Peter Mitchell's chemiosmosis theory on the

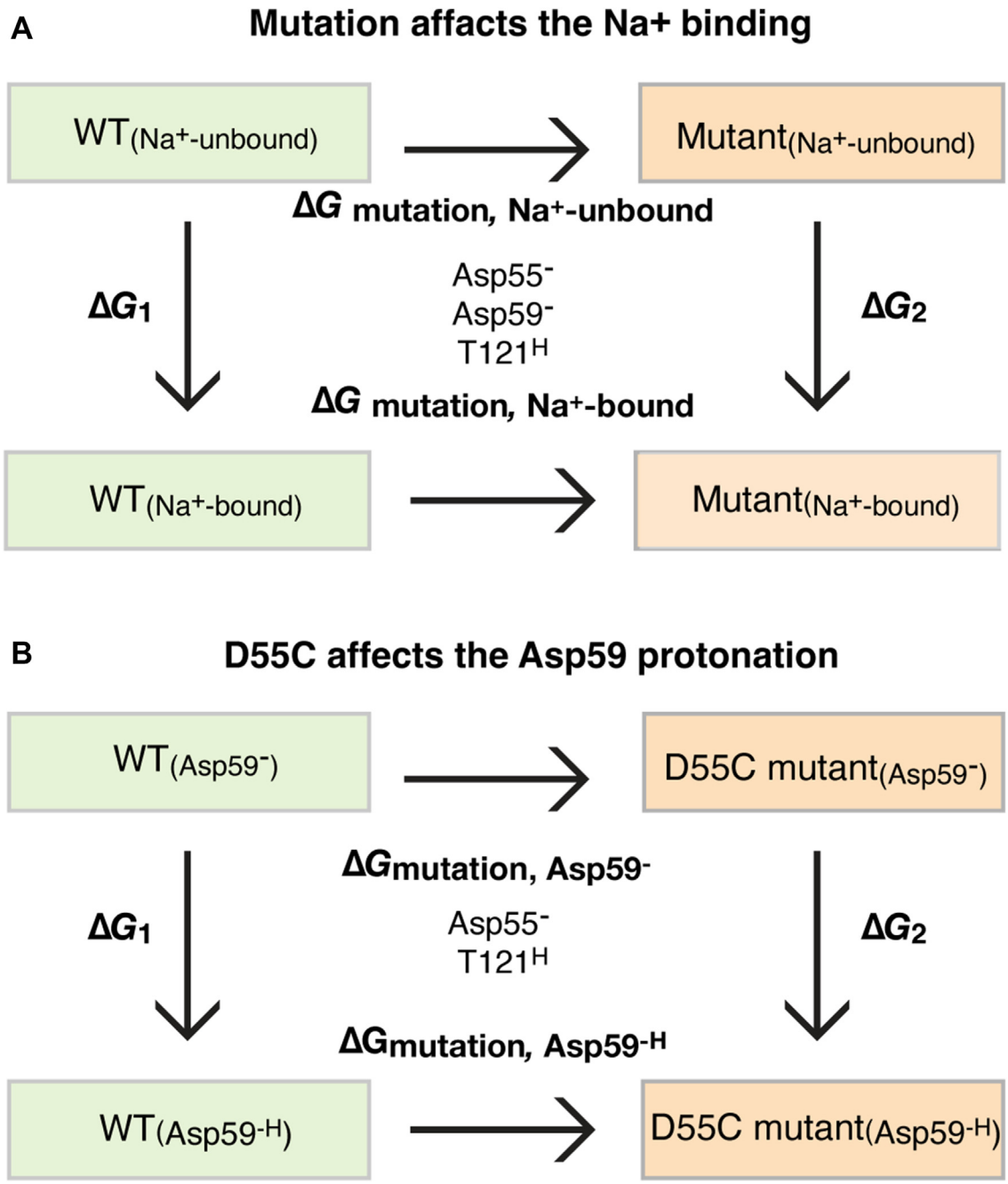

Figure 7. Thermodynamic cycle. The simulations were carried out as described in the Methods and the data were presented in Table 3. *A*, effect of mutation on the Na^+ binding; (*B*) effect of D55C mutation on the Asp59 protonation.

electrochemical H^+ gradient ($\tilde{\mu}_{H+}$), where a third term named transmembrane-electrically localized protons (TELP) was described (24, 25), in addition to Ψ and ΔpH. Accordingly, the transmembrane-electrically localized protons density is likely several magnitudes higher than the bulk solution H^+ concentration because the plasma membrane acts as a TELP-associated capacitor, where the intracellular negative charges (OH^-) transmembrane-electrostatically attract H^+ onto the periplasmic surface of the plasma membrane. This revision of the chemiosmosis theory can also explain the transport bioenergetics of the alkalophilic bacteria (25).

Together with the previous studies, the current structural and functional analysis, as well as the quantification of the energetic contributions of the individual residues in the MelB cation-binding pocket, clearly demonstrate that Asp55, Asp59, and Thr121 are critical for Na^+ binding, Asp55, and Asp59 are critical for Li^+ binding, and Asp59 is the sole H^+-binding site. Furthermore, our study also determined the membrane potential as the primary driving force for the H^+-coupled active melibiose transport mediated by MelB and provided the data to support the novel theory of TLEP (24).

Table 3
Mutation-induced free energy changes of Na^+ or H^+ binding ($\Delta\Delta G_{cation\text{-}binding}$)

Quantity	WT → D59C (kcal/mol)	WT → D55C (kcal/mol)	WT → T121A (kcal/mol)
$\Delta G_{mutation,\ Na+\text{-}unbound}$ [a]	117.2 ± 0.2	124.3 ± 0.2	15.89 ± 0.03
$\Delta G_{mutation,\ Na+\text{-}bound}$ [a]	127.7 ± 0.1	132.9 ± 0.2	22.5 ± 0.1
$\Delta\Delta G_{Na+\ binding}$ [b]	**10.5 ± 0.3**	**8.6 ± 0.4**	**6.7 ± 0.1**
$\Delta G_{mutation,\ Asp59^-}$ [a]		124.2 ± 0.1	
$\Delta G_{mutation,\ Asp59\text{-}H}$ [c]		126.2 ± 0.1	
$\Delta\Delta G_{proton\ binding\ at\ Asp59}$		**2.0 ± 0.2**	
$\Delta G_{mutation,\ Asp55^-}$ [a]	117.2 ± 0.2		
$\Delta G_{mutation,\ Asp55\text{-}H}$ [c]	122.2 ± 0.3		
$\Delta\Delta G_{proton\ binding\ at\ Asp55}$ [b]	**5.1 ± 0.4**		

The $\Delta\Delta G_{cation\text{-}binding}$ values were calculated by free energy perturbation (FEP) simulations. Based on the thermodynamic cycle depicted in Figure 7, $\Delta\Delta G_{cation\text{-}binding}$ equals the difference between the mutation-induced free energy changes calculated in two distinct states of the system: (1) MelB is bound with a cation ($\Delta G_{mutation,\ cation\text{-}unbound\ state}$) and (2) MelB is not bound with a cation ($\Delta G_{mutation,\ cation\text{-}bound\ state}$).
[a] $\Delta G_{mutation,\ cation\text{-}unbound\ state}$ reflects the free energy change induced by a mutation when $MelB_{St}$ is at a cation-free form, *i.e.*, unbound with the test cation (Na^+ or H^+).
[b] $\Delta\Delta G_{cation\text{-}binding} = \Delta G_{mutation,\ cation\text{-}bound\ state} - \Delta G_{mutation,\ cation\text{-}unbound\ state}$. $\Delta\Delta G_{cation\text{-}binding}$ reflects the change in the cation-binding free energy induced by a mutation. A more positive $\Delta\Delta G$ indicates a larger reduction in cation-binding affinity after the mutation.
[c] $\Delta G_{mutation,\ cation\text{-}bound\ state}$ reflects the free energy change induced by mutation when MelB is bound with the cation.

Experimental procedures

Reagents

[1-^{3}H]Melibiose (5.32 Ci/mmol) was custom synthesized by *PerkinElmer,* and unlabeled melibiose was purchased from *Acros Organics* (*Fisher Scientific*). 4-nitrophenyl-α-D-galactopyranoside (α-NPG) was purchased from *Sigma-Aldrich*. 2′-(*N*-dansyl)aminoalkyl-1-thio-β-D-galactopyranoside (D^2G) was gifted from Dr Gerard Leblanc. MacConkey agar media (lactose-free) was purchased from Difco. Detergents undecyl-β-D-maltopyranoside (UDM), dodecyl-β-D-maltopyranoside (DDM), and dodecyl-β-D-melibioside (DDMB) were purchased from *Anatrace*. *E. coli* lipids (Extract Polar, 100600) were purchased from *Avanti Polar Lipids, Inc*. All other materials were reagent grade and obtained from commercial sources.

Strains and plasmids construction

E. coli DW2 cells (*melA*$^+$, *melB*$^-$, *lacZ*$^-$*Y*$^-$) (34) were used for protein expression and functional studies. The expression plasmid pK95 ΔAH/$MelB_{St}$/$CHis_{10}$ was used for constitutively expressing the WT $MelB_{St}$ and $MelB_{St}$ mutant D55C and D59C (4, 7).

[1-^{3}H]Melibiose transport assay

E. coli DW2 cells transformed with a given plasmid were grown in Luria-Bertani (LB) broth with 100 mg/L ampicillin in a 37 °C shaker. The overnight cultures were diluted by 5% to fresh LB broth with 0.5% glycerol and 100 mg/L ampicillin and shaken at 30 °C for 5 h. The cells were washed with 50-ml 100 mM KP_i, pH 7.5 three times, followed by washing with the assay buffer (100 mM KP_i, pH 7.5, 10 mM $MgSO_4$). The cell pellets were resuspended and adjusted to A_{420} = 10 (∼0.7 mg proteins/ml) with the assay buffer. The transport assay was performed at 0.4 mM [^{3}H]melibiose (specific activity of 10 mCi/mmol) in the absence of Na^+ and Li^+ or the presence of Na^+ or Li^+ as described (4, 35) to test the three transport model coupling to H^+, Na^+, or Li^+, respectively. The transport time courses were carried out by quenching the cells at zero, 5 s, 10 s, 30 s, 1 m, 2 m, 5 m, 10 m, and 30 m by dilution and fast filtration. The filters were subjected to radioactivity measurements using a liquid scintillation counter.

The CCCP effect on the transport activity at varied pH conditions in the absence of Na^+ and Li^+ was conducted by incubating the extensively washed Na^+-free, Li^+-free cells with 10 μM CCCP for 10 min prior to the transport assay.

pH effect on transport activity

E. coli DW2 cells expressing the WT $MelB_{St}$, D55C, or D59C mutants were prepared as described above. After three washing using the Na^+-free buffer, the last washing and resuspending were performed using a specific pH-adjusted buffer. By altering the ratio of KH_2PO_4 and K_2HPO_4, the buffers were adjusted to 5.5 to 9.0 with an interval of 0.5 value. A small amount of Tris base was added to prepare the pH 9.0 solution.

Melibiose fermentation on MacConkey agar plates

E. coli DW2 cells were transformed with a plasmid carrying the WT or mutants and plated on MacConkey agar plates containing 30 mM melibiose, 100 mg/L of ampicillin, and incubated at 37 °C. After 18 h, the plates were viewed and photographed immediately using a Camera. Magenta-colored colonies, normal melibiose fermentation; yellow colonies, no melibiose fermentation due to poor transport.

$MelB_{St}$ protein expression and purification

Cell growth for the large-scale production of WT $MelB_{St}$ or the D55C and D59C mutants was carried out using the same expression vector and cell strain as used in the functional analyses (7, 36). Briefly, $MelB_{St}$ purification from membranes by cobalt-affinity chromatography (Talon Superflow Metal Affinity Resin, Takara) after extraction by 1.5% UDM. $MelB_{St}$ protein was eluted with 250 mM imidazole in a buffer containing 50 mM NaPi, pH 7.5, 200 mM NaCl, 0.035% UDM, and 10% glycerol and further dialyzed to change the buffer conditions accordingly.

Protein concentration determination

The Micro BCA Protein Assay (Pierce Biotechnology, Inc) was used to determine the protein concentrations.

Isothermal titration calorimetry

All ITC ligand-binding assays were performed with the TA Instruments (Nano-ITC device) as described (15), which yields the exothermic binding as a positive peak. In a typical experiment, the titrand ($MelB_{St}$) placed in the ITC Sample Cell was titrated with the specified titrant Na^+, Li^+, melibiose, or α-NPG (placed in the Syringe) in the assay buffer by an incremental injection of 2-μL aliquots at an interval of 300 s at a constant stirring rate of 250 rpm (nano-ITC). $MelB_{St}$ protein samples were buffer-matched to the assay buffer by dialysis. For measuring Na^+ or Li^+ binding, 100 mM choline chloride was supplemented into the Na^+-free buffer.

All samples were degassed using a TA Instruments Degassing Station (model 6326) for 15 min. During the titration, the heat changes were collected at 25 °C, and data processing was performed with the NanoAnalyze (version 3.7.5 software) provided with the instrument. The normalized heat changes were subtracted from the heat of dilution elicited by the last few injections, where no further binding occurred, and the corrected heat changes were plotted against the mole ratio of titrant *versus* titrand. The binding association constant (K_a) values were obtained by fitting the data using the one-site independent-binding model included in the NanoAnalyze software (version 3.7.5). The dissociation constant (K_d) = $1/K_a$.

Preparation of RSO vesicles

Right-Side-Out (RSO) membrane vesicles were prepared from *E. coli* DW2 cells overexpressing the WT or D55C $MelB_{St}$ by osmotic lysis (4, 37, 38). The concentrated RSO membrane vesicles at ∼20 mg/ml protein concentrations in a 100 mM KP_i buffer (pH 7.5) were diluted to a protein concentration of 1 mg/ml using 100 mM KPi at pH 6.0 or 8.0, respectively. The samples were incubated at 23 °C for 30 min prior to binding assay.

Galactoside-binding assay

Duplicate measurements of Trp→Dansyl galactoside (D^2G) FRET experiments were conducted using an Amico-Bowman Series 2 (AB2) Spectrofluorometer (4). An aliquot of 200 μl RSO vesicles at pH 6.0 or 8.0 was used to monitor the fluorescent changes. Trp residues were excited at 290 nm and emission of D^2G was recorded at 490 nm. On the time trace, the sequential additions of 10 μM D^2G, 50 mM NaCl, and >120 mM melibiose were carried out at 1-, 2- and 3-min time points, respectively.

Crystallization, native diffraction data collection, and processing

The purified D55C or D59C $MelB_{St}$ mutant in solutions were dialyzed overnight against the sugar-free dialysis buffer (consisting of 20 mM Tris-HCl, pH 7.5, 100 mM NaCl, 0.035% UDM, and 10% glycerol), concentrated with Vivaspin column at 50 kDa cutoff to approximately 30 to 50 mg/ml, and subjected to ultracentrifugation at 384,492*g* for 45 min at 4 °C (Beckman Coulter Optima MAX, TLA-100 rotor), stored at −80 °C after flash-frozen with liquid nitrogen for crystallization trials. A phospholipid stock solution at a concentration of approximately 20 mM was prepared by dissolving the *E. coli* Extract Polar (Avanti, 100600) with a dialysis buffer containing 0.01% DDM instead of 0.035% UDM.

Crystallization trials were carried out by the hanging-drop vapor-diffusion method at 23 °C by mixing 2-μL pre-treated protein samples with 2-μl reservoir. For the crystallization of the apo D59C $MelB_{St}$ mutant, the protein sample was diluted to a final concentration of 10 mg/ml with the same sugar-free dialysis buffer, supplemented with phospholipids at a concentration of approximately 3.6 mM from the 20-mM stock, and incubated for 15 min prior to the crystallization trials. The apo D59C mutant crystals appeared in 3 to 4 days against a reservoir consisting of 100 mM Tris-HCl, pH 8.5, 100 mM $NaCl_2$, 50 mM $CaCl_2$, and 32% PEG 400, and frozen with liquid nitrogen in 2 weeks, and tested for X-ray diffraction at the Lawrence Berkeley National Laboratory ALS BL 8.2.2 *via* remote data collection method.

For the crystallization of the DDMB-bound D55C $MelB_{St}$ mutant, the protein solution was diluted with the dialysis buffer to a final concentration of 10 mg/ml with the supplement of phospholipids at a concentration of approximate 3.6 mM from the 20-mM stock and 0.015% DDMB (1 x CMC) and 10% PEG 3350 and incubated for 15 min prior to the preparation of the crystallization drops. The crystals were grown using a reservoir consisting of MES, pH 6.5, 100 mM $NaCl_2$, 50 mM $CaCl_2$, 100 mM, and 32% PEG 400. Crystals appeared in 3 to 4 days, were frozen with liquid nitrogen in 3 weeks, and tested for X-ray diffraction at ALS BL 5.0.1 *via* remote data collection method. The complete diffraction datasets for the apo D59C and DDMB-bound D55C structures were collected at 100 K from a single cryo-cooled crystal at a wavelength of 1.0 Å on ALS BL 8.2.2 with an ADSC Quantum 315r detector or 0.97741 Å on ALS BL 5.0.1 with a Dectris Pilatus 2M detector, respectively. ALS auto-processing XDS or DIALS programs output files were further processed by AIMLESS in the ccp4i2 program for the structure solution (39). The statistics in data collection are described in Table 2.

Structure determination

The structure determination for the apo D59C and DDMB-bound D55C $MelB_{St}$ mutants was performed by molecular replacement method using the α-NPG-bound D59C $MelB_{St}$ mutant structure [PDB ID 7L17] as the search template, followed by rounds of manual building and refinement to resolutions of 3.18 Å [PDB ID 8FRH] or 3.0 Å [PDB ID 8QF9], respectively, using Phenix (40). The 3-D structure of DDMB (code, LMO) from the DDMB-bound D59C mutant [PDB ID 7L16] was used to fit and 10 carbon atoms were removed due to disorder. The apo D59C and DDMB-bound D55C structures were modeled from positions 2 to 454 or 2 to 456, respectively, without a gap. Both density maps showed a strong positive density with a sausage shape aligning with the helix

IX. A PEG molecule (ligand ID 1PE) was used to model for both structures. All structures are virtually identical.

There is an unknown denticity blob in the sugar-binding pocket of the apo D59C structure, which is too small to fit even by a monosaccharide. It might be fit by a glycerol molecule. The statistics of refinement for the final models are summarized in Table 2. For apo and DDMB-bound structures: Ramachandran favored of 95.57% and 94.04%, Ramachandran outliers of 0% and 0.44%, clash scores of 1.38 and 2.18, and overall scores of 1.18 and 1.55, respectively, as judged by MolProbity in Phenix. Pymol (2.5.2) was used to generate all graphs (http://www.pymol.org/pymol).

MD simulations

The initial configuration for our simulations was derived from the crystal structure of the D55C mutant of $MelB_{St}$. For WT system setup, the Asp55 was reverted to a deprotonated state. For the D55C mutant setup, the protein structure was used directly. For the D59C mutant setup, the Asp55 was reverted to a deprotonated state, and the Asp59 was mutated to Cys. For the T121A mutant setup, the Asp59 was deprotonated, and the Thr121 was mutated to Ala. For all of the systems, the Asp59 and Asp55 residues were deprotonated whenever applicable, while other ionizable residues maintained their standard protonation states (deprotonated Asp, Glu, His, and protonated Thr, Ser, Cys, Lys, Arg, Tyr). In the initial setups of all three titratable systems, a melibiose molecule was positioned within the sugar-binding site based on the crystal structure of α-NPG, and a Na^+ ion was positioned between Asp59 and Asp55 in the crystal structure. The protein was integrated into a lipid bilayer composed of a 7:2 ratio of POPE to POPG, mirroring the *E. coli* membrane composition, with a total of 288 lipid molecules. Water molecules enveloped both sides of the lipid bilayer, and a solution with an approximate concentration of 0.15 M was created by introducing NaCl ions among the water molecules. The simulation system encompassed approximately 121,000 atoms, and the periodic boundary condition was set at approximately 100 Å × 100 Å × 123 Å. The CharmmGUI web interface (41) was utilized to construct the system.

The system was equilibrated through the following procedure. Initially, the systems were relaxed through geometry optimization, with harmonic restraints (500 kJ/mol/Å^2 force constant) applied to the heavy atoms of the protein and lipids. Subsequently, a 250 ps simulation at a temperature of 303.15 K was conducted in the constant NVT ensemble. The temperature of the system was maintained using a Langevin thermostat with a friction coefficient of 1 ps^{-1}. The restraints were then systematically diminished to zero during 2 ns of dynamics in the constant NPT ensemble at 303.15 K and 1 atm pressure. The pressure of the system was maintained using the Langevin piston Nose-Hoover method (42, 43) piston pressure. A 200 ns production trajectory was generated in the constant NPT ensemble, maintaining the same temperature and pressure., and a 2 fs timestep was employed to propagate the trajectory, with constraints on bond lengths involving hydrogen atoms. The CHARMM36 force field (44–47) was employed for the protein, lipids, and melibiose, and the TIP3P model for water molecules (48). Electrostatic interactions were computed using the particle mesh Ewald method (49) with a 12 Å cutoff for van der Waals interactions. All MD simulations were performed using the NAMD software package (50).

FEP simulations

To assess the alteration in binding free energy resulting from mutations, we conducted free-energy perturbation (FEP) simulations for each mutant paired with the WT, namely WT ↔ D59C, WT ↔ D55C, and WT ↔ T121A. In each FEP simulation, the side chain of the mutated residue was systematically transitioned from its original type to the new one by gradually modifying the system's Hamiltonian using a λ parameter ranging from 0 to 1. Essentially, the λ parameter serves to linearly interpolate between the Hamiltonians of the WT system and the mutant. Equation 1 describes the Hamiltonian of the system undergoing mutation.

$$\mathscr{H}(x,p;\ \lambda)=\lambda\mathscr{H}(x,p;\mathrm{WT})+(1-\lambda)\mathscr{H}(x,p;\mathrm{mutant}) \quad (1)$$

As λ progresses from 0 to 1, the system's Hamiltonian undergoes a gradual transition from the description of one variant of $MelB_{St}$ (*e.g.*, WT) to another (*e.g.*, mutant). From each FEP simulation, we extracted the free energy change (ΔG) for the entire system resulting from the mutation, in both the cation-unbound and cation-bound states of $MelB_{St}$, yielding $\Delta G_{\mathrm{mutation,\ cation-unbound\ state}}$ and $\Delta G_{\mathrm{mutation,\ cation-bound\ state}}$, respectively. The melibiose molecule remained bound with the protein throughout the simulation.

Subsequently, we construct a thermodynamic cycle (Fig. 7), allowing us to calculate the difference in the cation binding free energies (Na^+ or proton) between the mutant and WT (Equation 1):

$$\Delta\Delta G_{cation\ binding}=\Delta G_2-\Delta G_1=\Delta G_{\mathrm{mutation,\ cation-bound\ state}}-\Delta G_{\mathrm{mutation,\ cation-unbound\ state}} \quad (2)$$

A positive $\Delta\Delta G$ indicates a decrease in binding affinity upon mutation. In the context of proton binding affinity for a specific residue, the terms "cation-bound" and "cation-unbound" can be alternatively replaced with "protonated" and "deprotonated" states of the residue, respectively.

To reduce the statistical uncertainty in the calculated $\Delta\Delta G$, for every mutation pair in each condition (cation-bound or unbound), we conducted FEP simulations in both forward and backward directions, *i.e.*, WT → mutant and mutant → WT. This approach enables the application of the simple overlap sampling (SOS) technique for the estimation of $\Delta G_{\mathrm{mutation,\ cation-bound\ state}}$ or $\Delta G_{\mathrm{mutation,\ cation-unbound\ state}}$ along with their error bars. The free energy change within each window of the FEP was calculated using Equation 3. The simulations were carried out under isothermal and isobaric

conditions (constant pressure and temperature, *i.e.*, NPT ensemble).

$$\exp(-\beta\Delta G_{i\to i+1}) = \frac{\langle exp\left\{-\frac{\beta}{2}[\mathscr{H}(x,p;\ \lambda_{i+1}) - \mathscr{H}(x,p;\ \lambda_i)]\right\}\rangle_i}{\langle exp\left\{-\frac{\beta}{2}[\mathscr{H}(x,p;\ \lambda_i) - \mathscr{H}(x,p;\ \lambda_{i+1})]\right\}\rangle_{i+1}} \quad (3)$$

where $\Delta G_{i\to i+1}$ represents the Gibbs free energy change when the system transitions from the state represented with $\lambda = \lambda_i$ to $\lambda = \lambda_{i+1}$, $\mathscr{H}(x,p;\ \lambda_{i+1}) - \mathscr{H}(x,p;\ \lambda_i)$ denotes the energy difference between the two Hamiltonians with $\lambda = \lambda_i$ and $\lambda = \lambda_{i+1}$, at coordinates (x) and momenta (p) for all atoms in the system, and $\langle \ldots \rangle$ indenotes ensemble averages. In the forward run, the coordinates (x) and momenta (p) sampled under $\mathscr{H}(x,p;\lambda_i)$ are used to calculate $\mathscr{H}(x,p;\lambda_{i+1}) - \mathscr{H}(x,p;\ \lambda_i)$ at each snapshot. In the backward run, the x's and p's sampled under $\mathscr{H}(x,p;\lambda_{i+1})$ are used to calculate $\mathscr{H}(x,p;\lambda_i) - \mathscr{H}(x,p;\ \lambda_{i+1})$ at each selected snapshot. The parameter β is defined as $1/k_BT$, where k_B and T denote Boltzmann's constant and absolute temperature, respectively.

In each FEP run for the mutation process, we simulated 20 windows with λ values gradually transitioning from 0 to 1 for the forward run or 1 to 0 for the backward run, using a 0.05 interval. Within each window, we conducted 5 ns sampling, resulting in a total sampling time of 100 ns for each FEP run in each direction (forward or backward). This process was repeated for both forward and backward directions for each of the two cation-bound states, totaling 400 ns for each mutation-free-energy calculation. The initial structures for all FEP simulations were equilibrated for at least 10 ns in the corresponding cation-binding states (Table 1), following the original 200 ns MD equilibration described above. The total FEP simulation time was ∼2 μs for all systems.

PROPKA calculations of the pKa value of Asp55 and Asp59 residues

The absolute pKa values of Asp55 and Asp59 in the WT mutants were estimated using the PROPKA program (51, 52). For each system, 2000 snapshots were selected from the three 200 ns MD production trajectories with a 0.1 ns interval. For each snapshot, the pKa values of the Asp59 and Asp55 were calculated, and the results are averaged over all snapshots. Consistent with the simulation procedure used in ref. (14), for the estimation of Asp55's pKa, the Asp59 residue was deprotonated and Asp55 was protonated throughout the MD simulation. For the estimation of Asp59's pKa, the Asp59 residue was protonated and Asp55 is deprotonated in the simulation. No Na^+ was present in the cation-binding site in all simulations.

Statistics and reproducibility

All experiments were performed 2 to 4 times. The average values were presented in the table with standard errors. An unpaired t test was used for statistical analysis.

Data availability

The x-ray diffraction datasets and models have been deposited to wwPDB under the accession code 8FQ9 for D55C $MelB_{St}$ with DDMB and 8FRH for D59C $MelB_{St}$ at an apo state.

Supporting information—This article contains supporting information.

Acknowledgments—We thank Gerard Leblanc for a MelB-expressing vector, the DW2 strain, and the dansyl galactoside. The x-ray diffraction datasets for the apo D59C and DDMB-bound D55C structures were collected at ALS BL 8.2.2 and 5.0.1, respectively. This work was supported by the National Institutes of Health Grant R01 GM122759 to L. G. and R35 GM150780 and Welch Foundation D-2108-20220331 to R. L. The content is solely the responsibility of the authors and does not necessarily represent the official views of the National Institutes of Health.

Author contributions—L. G. and R. L. conceptualization; L. G., P. H., R. L., and A. B. data curation; L. G., P. H., and R. L. formal analysis; L. G. and R. L. funding acquisition; L. G., P. H., R. L., and A. B. investigation; L. G. and R. L. supervision; L. G., P. H., and R. L. validation; L. G. visualization; L. G., R. L., and A. B. writing–original draft, L. G. and R. L. writing–review & editing; P. H. Methodology.

Conflict of interest—The authors declare that they have no known competing financial interests or personal relationships that could have appeared to influence the work reported in this paper.

Abbreviations—The abbreviations used are: α-NPG, 4-nitrophenyl-α-D-galactopyranoside; $\Delta G_{\text{mutation, cation-bound state}}$, reflects the free energy change introduced by a mutation when $MelB_{St}$ is at a cation-bound form; $\Delta G_{\text{mutation, cation-unbound state}}$, reflects the free energy change introduced by a mutation when $MelB_{St}$ is at a cation-free form; $\Delta\Delta G_{\text{cation-binding}}$, free energy change for a cation binding upon a mutation; D^2G, 2′-(*N*-dansyl)aminoalkyl-1-thio-β-D-galactopyranoside; FEP, free-energy perturbation; FRET, fluorescence resonance energy transfer; ITC, isothermal titration calorimetry; MFS, major facilitator superfamily; RSO membrane vesicle, right-side-out membrane vesicle; TELP, transmembrane-electrostatically localized protons.

References

1. Wilson, T. H., and Ding, P. Z. (2001) Sodium-substrate cotransport in bacteria. *Biochim. Biophys. Acta* **1505**, 121–130
2. Maehrel, C., Cordat, E., Mus-Veteau, I., and Leblanc, G. (1998) Structural studies of the melibiose permease of *Escherichia coli* by fluorescence resonance energy transfer. I. Evidence for ion-induced conformational change. *J. Biol. Chem.* **273**, 33192–33197
3. Meyer-Lipp, K., Sery, N., Ganea, C., Basquin, C., Fendler, K., and Leblanc, G. (2006) The inner interhelix loop 4-5 of the melibiose permease from *Escherichia coli* takes part in conformational changes after sugar binding. *J. Biol. Chem.* **281**, 25882–25892
4. Guan, L., Nurva, S., and Ankeshwarapu, S. P. (2011) Mechanism of melibiose/cation symport of the melibiose permease of *Salmonella typhimurium*. *J. Biol. Chem.* **286**, 6367–6374
5. Granell, M., Leon, X., Leblanc, G., Padros, E., and Lorenz-Fonfria, V. A. (2010) Structural insights into the activation mechanism of melibiose permease by sodium binding. *Proc. Natl. Acad. Sci. U. S. A.* **107**, 22078–22083

6. Guan, L. (2018) Na(+)/Melibiose Membrane Transport Protein, MelB In. In: Roberts, G., Watts, A., eds. *European Biophysical Societies (eds) Encyclopedia of Biophysics*, 2nd Ed, Springer, Berlin, Heidelberg
7. Ethayathulla, A. S., Yousef, M. S., Amin, A., Leblanc, G., Kaback, H. R., and Guan, L. (2014) Structure-based mechanism for Na(+)/melibiose symport by MelB. *Nat. Commun.* **5**, 3009
8. Guan, L., and Hariharan, P. (2021) X-ray crystallography reveals molecular recognition mechanism for sugar binding in a melibiose transporter MelB. *Commun. Biol.* **4**, 931
9. Nguyen, L. N., Ma, D., Shui, G., Wong, P., Cazenave-Gassiot, A., Zhang, X., *et al.* (2014) Mfsd2a is a transporter for the essential omega-3 fatty acid docosahexaenoic acid. *Nature* **509**, 503–506
10. Chua, G. L., Tan, B. C., Loke, R. Y. J., He, M., Chin, C. F., Wong, B. H., *et al.* (2023) Mfsd2a utilizes a flippase mechanism to mediate omega-3 fatty acid lysolipid transport. *Proc. Natl. Acad. Sci. U. S. A.* **120**, e2215290120
11. Hariharan, P., Shi, Y., Katsube, S., Willibal, K., Burrows, N. D., Mitchell, P., *et al.* (2024) Mobile barrier mechanisms for Na(+)-coupled symport in an MFS sugar transporter. *Elife* **12**, RP92462
12. Guan, L. (2023) The rapid developments of membrane protein structure biology over the last two decades. *BMC Biol.* **21**, 300
13. Cater, R. J., Chua, G. L., Erramilli, S. K., Keener, J. E., Choy, B. C., Tokarz, P., *et al.* (2021) Structural basis of omega-3 fatty acid transport across the blood-brain barrier. *Nature* **595**, 315–319
14. Katsube, S., Liang, R., Amin, A., Hariharan, P., and Guan, L. (2022) Molecular basis for the cation selectivity of Salmonella typhimurium melibiose permease. *J. Mol. Biol.* **434**, 167598
15. Hariharan, P., and Guan, L. (2017) Thermodynamic cooperativity of cosubstrate binding and cation selectivity of *Salmonella typhimurium* MelB. *J. Gen. Physiol.* **149**, 1029–1039
16. [preprint] Hariharan, P., Shi, Y., Katsube, S., Willibal, K., Burrows, N. D., Mitchell, P., *et al.* (2023) Mobile barrier mechanisms for Na(+)-coupled symport in an MFS sugar transporter. *bioRxiv*. https://doi.org/10.1101/2023.09.18.558283
17. Pourcher, T., Bassilana, M., Sarkar, H. K., Kaback, H. R., and Leblanc, G. (1990) The melibiose/Na+ symporter of *Escherichia coli*: kinetic and molecular properties. *Philos. Trans. R. Soc. Lond. B Biol. Sci.* **326**, 411–423
18. Guan, L., and Kaback, H. R. (2006) Lessons from lactose permease. *Annu. Rev. Biophys. Biomol. Struct.* **35**, 67–91
19. Guan, L., Jakkula, S. V., Hodkoff, A. A., and Su, Y. (2012) Role of Gly117 in the cation/melibiose symport of MelB of *Salmonella typhimurium*. *Biochemistry* **51**, 2950–2957
20. Hariharan, P., and Guan, L. (2014) Insights into the inhibitory mechanisms of the regulatory protein IIA(Glc) on melibiose permease activity. *J. Biol. Chem.* **289**, 33012–33019
21. Zani, M. L., Pourcher, T., and Leblanc, G. (1993) Mutagenesis of acidic residues in putative membrane-spanning segments of the melibiose permease of *Escherichia coli*. II. Effect on cationic selectivity and coupling properties. *J. Biol. Chem.* **268**, 3216–3221
22. Zani, M. L., Pourcher, T., and Leblanc, G. (1994) Mutation of polar and charged residues in the hydrophobic NH2-terminal domains of the melibiose permease of *Escherichia coli*. *J. Biol. Chem.* **269**, 24883–24889
23. Markham, K. J., Tikhonova, E. B., Scarpa, A. C., Hariharan, P., Katsube, S., and Guan, L. (2021) Complete cysteine-scanning mutagenesis of the Salmonella typhimurium melibiose permease. *J. Biol. Chem.* **297**, 101090
24. Lee, J. W. (2020) Isothermal Environmental heat energy Utilization by transmembrane electrostatically localized protons at the liquid-membrane interface. *ACS Omega* **5**, 17385–17395
25. Lee, J. W. (2021) Mitochondrial energetics with transmembrane electrostatically localized protons: do we have a thermotrophic feature? *Sci. Rep.* **11**, 14575
26. Guan, L. (2022) Structure and mechanism of membrane transporters. *Sci. Rep.* **12**, 13248
27. Franco, P. J., Jena, A. B., and Wilson, T. H. (2001) Physiological evidence for an interaction between helices II and XI in the melibiose carrier of Escherichia coli. *Biochim. Biophys. Acta* **1510**, 231–242
28. Slonczewski, J. L., Rosen, B. P., Alger, J. R., and Macnab, R. M. (1981) pH homeostasis in Escherichia coli: measurement by 31P nuclear magnetic resonance of methylphosphonate and phosphate. *Proc. Natl. Acad. Sci. U. S. A.* **78**, 6271–6275
29. Padan, E., and Schuldiner, S. (1986) Intracellular pH regulation in bacterial cells. *Methods Enzymol.* **125**, 337–352
30. Fluman, N., Ryan, C. M., Whitelegge, J. P., and Bibi, E. (2012) Dissection of mechanistic principles of a secondary multidrug efflux protein. *Mol. Cell* **47**, 777–787
31. Mitchell, P. (1961) Coupling of phosphorylation to electron and hydrogen transfer by a chemi-osmotic type of mechanism. *Nature* **191**, 144–148
32. Mitchell, P. (1968) *Chemiosmotic Coupling and Energy Transduction*, Glynn Research Ltd, Bodmin, England
33. Felle, H., Porter, J. S., Slayman, C. L., and Kaback, H. R. (1980) Quantitative measurements of membrane potential in *Escherichia coli*. *Biochemistry* **19**, 3585–3590
34. Botfield, M. C., and Wilson, T. H. (1988) Mutations that simultaneously alter both sugar and cation specificity in the melibiose carrier of Escherichia coli. *J. Biol. Chem.* **263**, 12909–12915
35. Jakkula, S. V., and Guan, L. (2012) Reduced Na(+) affinity increases turnover of *Salmonella enterica* serovar Typhimurium MelB. *J. Bacteriol.* **194**, 5538–5544
36. Pourcher, T., Leclercq, S., Brandolin, G., and Leblanc, G. (1995) Melibiose permease of *Escherichia coli*: large scale purification and evidence that H(+), Na(+), and Li(+) sugar symport is catalyzed by a single polypeptide. *Biochemistry* **34**, 4412–4420
37. Kaback, H. R. (1974) Transport in isolated bacterial membrane vesicles. *Methods Enzymol.* **31**, 698–709
38. Short, S. A., Kaback, H. R., and Kohn, L. D. (1974) D-lactate dehydrogenase binding in *Escherichia coli dld-* membrane vesicles reconstituted for active transport. *Proc. Natl. Acad. Sci. U. S. A.* **71**, 1461–1465
39. Potterton, L., Agirre, J., Ballard, C., Cowtan, K., Dodson, E., Evans, P. R., *et al.* (2018) CCP4i2: the new graphical user interface to the CCP4 program suite. *Acta Crystallogr. D Struct. Biol.* **74**, 68–84
40. Adams, P. D., Afonine, P. V., Bunkoczi, G., Chen, V. B., Davis, I. W., Echols, N., *et al.* (2010) PHENIX: a comprehensive Python-based system for macromolecular structure solution. *Acta Crystallogr. D Biol. Crystallogr.* **66**, 213–221
41. Jo, S., Kim, T., Iyer, V. G., and Im, W. (2008) CHARMM-GUI: a web-based graphical user interface for CHARMM. *J. Comput. Chem.* **29**, 1859–1865
42. Martyna, G., Tobias, D., and Klein, M. (1994) Constant pressure molecular dynamics algorithms. *J. Chem. Phys.* **101**, 4177–4189
43. Feller, S., Zhang, Y., Pastor, R., and Brooks, B. (1995) Constant pressure molecular dynamics simulation: the Langevin piston method. *J. Chem. Phys.* **103**, 4613–4621
44. Beglov, D., and Roux, B. (1994) Finite representation of an infinite bulk system: solvent boundary potential for computer simulations. *J. Chem. Phys.* **100**, 9050–9063
45. Klauda, J. B., Venable, R. M., Freites, J. A., O'Connor, J. W., Tobias, D. J., Mondragon-Ramirez, C., *et al.* (2010) Update of the CHARMM all-atom additive force field for lipids: validation on Six lipid Types. *J. Phys. Chem. B* **114**, 7830–7843
46. Best, R. B., Zhu, X., Shim, J., Lopes, P. E. M., Mittal, J., Feig, M., *et al.* (2012) Optimization of the additive CHARMM all-atom protein force field Targeting improved sampling of the Backbone phi, psi and side-chain chi(1) and chi(2) Dihedral Angles. *J. Chem. Theory Comput.* **8**, 3257–3273
47. Guvench, O., Hatcher, E., Venable, R. M., Pastor, R. W., and MacKerell, A. D. (2009) CHARMM additive all-atom force field for Glycosidic Linkages between Hexopyranoses. *J. Chem. Theory Comput.* **5**, 2353–2370
48. Jorgensen, W. L., Chandrasekhar, J., Madura, J. D., Impey, R. W., and Klein, M. L. (1983) Comparison of simple potential Functions for simulating liquid water. *J. Chem. Phys.* **79**, 926–935
49. Darden, T., York, D., and Pedersen, L. (1993) Particle mesh Ewald: an N·log(N) method for Ewald sums in large systems. *J. Chem. Phys.* **98**, 10089–10092

50. Eastman, P., Friedrichs, M. S., Chodera, J. D., Radmer, R. J., Bruns, C. M., Ku, J. P., *et al.* (2013) OpenMM 4: a Reusable, extensible, Hardware independent Library for high performance molecular simulation. *J. Chem. Theory Comp.* **9**, 461–469
51. Sondergaard, C. R., Olsson, M. H., Rostkowski, M., and Jensen, J. H. (2011) Improved Treatment of ligands and coupling effects in Empirical calculation and Rationalization of pKa values. *J. Chem. Theory Comput.* **7**, 2284–2295
52. Olsson, M. H., Sondergaard, C. R., Rostkowski, M., and Jensen, J. H. (2011) PROPKA3: consistent Treatment of internal and surface residues in Empirical pKa Predictions. *J. Chem. Theory Comput.* **7**, 525–537